Exclusive measurements of $\pi^{\pm}p \rightarrow \pi^{+}\pi^{\pm}n$ near threshold

M. Kermani,[1] P. A. Amaudruz,[4] F. Bonutti,[2,3] J. T. Brack,[4,*] P. Camerini,[2,3] L. Felawka,[4] E. Fragiacomo,[2,3] E. F. Gibson,[5] N. Grion,[2] G. J. Hofman,[1,*] R. R. Johnson,[1] E. L. Mathie,[6] S. McFarland,[1] R. Meier,[4,†] D. Ottewell,[4] K. J. Raywood,[1] R. Rui,[2,3] M. E. Sevior,[7] G. R. Smith,[4,‡] and R. Tacik[6]

(The CHAOS Collaboration)

[1]*Physics Department, University of British Columbia, Vancouver, British Columbia, Canada V6T 2A6*

[2]*Istituto Nazionale di Fisica Nucleare, 34127 Trieste, Italy*

[3]*Dipartimento di Fisica dell'Universita' di Trieste, 34127 Trieste, Italy*

[4]*TRIUMF, Vancouver, British Columbia, Canada V6T 2A3*

[5]*California State University, Sacramento, California 95819*

[6]*University of Regina, Regina, Saskatchewan, Canada S4S 0A2*

[7]*School of Physics, University of Melbourne, Parkville, Victoria, 3052, Australia*

(Received 3 June 1998)

The pion induced pion production reactions $\pi^{\pm}p \rightarrow \pi^{+}\pi^{\pm}n$ were studied at projectile incident energies of 223, 243, 264, 284, and 305 MeV, using a cryogenic liquid hydrogen target. The Canadian High Acceptance Orbit Spectrometer was used to detect the two outgoing pions in coincidence. The experimental results are presented in the form of single differential cross sections. Total cross sections obtained by integrating the differential quantities are also reported. In addition, the invariant mass distributions from the $(\pi^{+}\pi^{-})$ channel were fitted to determine the parameters for an extended model based on that of Oset and Vicente-Vacas. We find the model parameters obtained from fitting the $(\pi^{+}\pi^{-})$ data do not describe the invariant mass distributions in the $(\pi^{+}\pi^{+})$ channel. [S0556-2813(98)00112-5]

PACS number(s): 13.75.Lb, 13.60.Hb, 13.60.Le, 13.75.Gx

I. INTRODUCTION

It was Weinberg who first suggested [1] that the reaction $\pi N \rightarrow \pi\pi N$ may be used as a probe of $\pi\pi$ scattering. Among the processes contributing to the reaction $\pi N \rightarrow \pi\pi N$ is the one pion exchange mechanism (OPE), which accounts for the interaction of an off-shell pion with the physical pion. Although the OPE mechanism may be used to study $\pi\pi$ interactions, other processes such as resonance exchanges also contribute to the reaction amplitude. This presents theoretical difficulties as well as potential ambiguities in extracting $\pi\pi$ scattering observables from $\pi N \rightarrow \pi\pi N$ data.

Although work is in progress [2] to extend the predictive range of chiral perturbation theory (ChPT) well above the $\pi N \rightarrow \pi\pi N$ threshold, presently the connection between theory and experiment is reliable only at threshold. On the other hand, a study of the background (non-OPE) mechanisms, which also contribute at threshold, is best suited to the near threshold region. Constraints for the effective couplings of these background mechanisms can only be obtained by comparing a broad set of experimental results with the predictions of theoretical models.

In the present experiment, exclusive measurements of the $\pi^{\pm}p \rightarrow \pi^{+}\pi^{\pm}n$ reactions are reported in the near threshold region, at $T_{\pi}=223$, 243, 263, 285, and 305 MeV. The threshold for these reactions is at $T_{\pi}=172.4$ MeV. Total and single differential cross sections are reported, and interpreted within the framework of a microscopic model of the $\pi N \rightarrow \pi\pi N$ reaction first developed by Oset *et al.* [3] and later extended by Sossi *et al.* [4,5]. The measured invariant mass distributions for the $\pi^{+}\pi^{-}$ channel were fit to determine the model parameters (coupling constants for isobar exchanges which contribute to the non-OPE background). A separate publication [6,7] will deal with the double differential cross sections, Chew-Low and dispersion analyses, and extraction of the $\pi\pi$ scattering length obtained from these experimental results. The present work is organized as follows. Section II summarizes previous experiments. Section III describes the experimental apparatus. The techniques used in the data reduction process are described in Sec. IV. The results of the experiment are presented in Sec. V. The model is introduced in Sec. VI, and the data are compared to the model results there. Conclusions are summarized in Sec. VII.

II. PREVIOUS $\pi N \rightarrow \pi\pi N$ EXPERIMENTS

There are five different experimentally accessible channels of elementary pion induced pion production on the proton. These are $\pi^{\pm}p \rightarrow \pi^{+}\pi^{\pm}n$, $\pi^{\pm}p \rightarrow \pi^{\pm}\pi^{0}p$, and $\pi^{-}p \rightarrow \pi^{0}\pi^{0}n$. In the past, the above reactions have been studied over a wide range of incident pion energies. However, only the near threshold [8–18] measurements ($T_{\pi} \leq 400$ MeV) are of interest in the current work.

In 1974 Jones *et al.* measured angular distributions in the $(\pi^{+}\pi^{-})$ and $(\pi^{-}\pi^{0})$ channels at an incident pion momentum of 415 MeV/c [8]. They employed a 180 liter hydrogen

*Present address: University of Colorado, Boulder, CO 80309.

†Present address: Physikalisches Institut, Universität Tübingen, 72076 Tübingen, Germany.

‡Corresponding author. Electronic address: smith@triumf.ca

bubble chamber at Saturne. Out of 140 000 pictures taken, 881 ($\pi^+\pi^-$) and 140 ($\pi^-\pi^0$) events were detected.

In the late 1980's and early 1990's the Omicron group at CERN measured total cross sections and angular distributions for the ($\pi^+\pi^-$), ($\pi^-\pi^0$), and ($\pi^+\pi^+$) channels at incident pion momenta between 295 and 450 MeV/c [9–11]. These experiments employed a large solid angle magnetic spectrometer and a thin gas target. For each reaction the two charged particles in the final state were detected. In order to determine total cross sections, the angular distributions were extrapolated to the regions of phase space not covered by the experimental apparatus. They assumed that all kinematic variables except the dipion invariant mass in the ($\pi^+\pi^-$) channel were distributed according to phase space. These data have been criticized for the limited phase-space coverage as well as the extrapolation process used to determine total cross sections.

In 1993, Sevior *et al.* reported total cross section measurements performed at TRIUMF. The ($\pi^+\pi^+$) channel was studied at incident pion energies of 180, 184, 190, and 200 MeV [12,13]. They used a novel method in which a set of 5 thin plastic scintillators were employed as active targets in which the final state pions were detected. An array of neutron detectors was used to detect the final state neutron. The same group has recently reported measurements in both the ($\pi^+\pi^+$) and ($\pi^+\pi^-$) channels [14]. To date, these represent the experimental data acquired closest to the pion production threshold energy. The measured cross sections of Sevior *et al.* are in disagreement with those obtained by the Omicron group.

At PSI, the Erlangen group performed exclusive measurements of the ($\pi^+\pi^-$) channel at pion incident energies of 247, 284, and 330 MeV with a liquid hydrogen target [15]. They employed a magnetic spectrometer, plastic scintillators and wire chambers in order to cover large regions of phase space, including regions out-of-plane. The published results were in the form of pion-pion angular correlations, and triple differential cross sections at 1301 MeV total center-of-mass energy. No total cross sections were published.

Measurements of the ($\pi^0\pi^0$) channel at pion incident energies ranging from 5 MeV above threshold to $T_\pi = 293$ MeV were performed by Lowe *et al.* at Brookhaven [16]. They used the crystal box detector to acquire kinematically complete data over a large region of phase space. In this experiment the four final state photons originating from π^0 decay were detected, and the $\pi^0\pi^0$ events were isolated by reconstructing the missing mass of the final state neutron.

In 1993, the Virginia group measured total cross sections as well as angular distributions at LAMPF for the ($\pi^+\pi^0$) channel at incident pion energies of 190, 200, 220, 240, and 260 MeV [17,18]. They employed a π^0 spectrometer and a charged particle detector, and performed an analysis in which all of the existing $\pi N \rightarrow \pi\pi N$ data were fitted to extract partial amplitudes in the framework of the Olssen and Turner (OT) model [19].

The above constitutes a large body of threshold $\pi\pi N$ data, but the only published differential cross sections are at a single incident pion energy [15]. The published angular distributions from other works are often in arbitrary units [8,9]. As such, it is difficult to interpret these data in the context of a model or even to make direct comparisons of the experimental results.

III. THE EXPERIMENT

The experiment was performed using the M11 pion beam line at TRIUMF. The TRIUMF cyclotron provided a 140 μA, 500 MeV proton beam with a 100% duty factor. The primary proton beam was composed of 3–4 ns wide buckets every 43 ns. Pions were produced on a 10 mm thick graphite production target.

A. Pion channel

Slits and jaws in the front-end of the M11 channel were used to adjust the intensity of the beam transported to the focus, approximately 14 m from the production target. In this experiment, the pion flux was typically 1 MHz for incident π^- and 2.5 MHz for incident π^+. Slits situated at the dispersed intermediate focus of the channel (18mm/%$\Delta p/p$) were adjusted such that the momentum spread $\Delta p/p$ of the incident π^+ (π^-) beam was 1% (5%). The momentum distribution of the channel is uniform with centroid p, and standard deviation Δp. For the case of the relatively wide π^- momentum acceptance, a 16 element scintillation counter hodoscope consisting of 6 mm wide strips each 1.6 mm thick was employed. This reduced the uncertainty in the momentum of the incident π^- to $\sim$0.3%. The hodoscope was not used for incident π^+, due to the heavy proton contamination at the midplane of the channel. The proton contamination was mitigated by means of an absorber (typically 6 mm thick CH_2) at the channel mid-plane. With the absorber, the π:p ratio was typically 3:1 at the final focus of the channel. At the energies studied in this experiment, the $\mu^\pm$ and $e^\pm$ contamination was small ($\leqslant$2%).

B. The target

A liquid hydrogen target was used for the experiment. The liquid hydrogen was contained in a cylindrical target cell of radius 25.5 mm and height 50 mm. The cell consisted of 0.125 mm thick Mylar held in place by copper disks 54 mm in diameter at the top and bottom of the cell. The cell was surrounded by vacuum, and a 0.007 mm thick aluminum heat shield at a radius of 29.6 mm. The outside pressure was supported by a Mylar foil wrapped around a honeycomb structure located at an outer radius of 46.8 mm.

The target temperature was determined [20] by measuring the vapor pressure of the liquid hydrogen in the target cell. The nominal operating temperature of the target was 18 K. At this temperature the liquid hydrogen density is 0.074 g/cm^3 [20].

C. Beam counting

Incident pions were counted using two plastic scintillators situated between the end of the channel and the entrance of the spectrometer. The first counter S_1 was placed approximately 1.5 m upstream of the final focus and consisted of four adjacent 10 cm wide horizontal strips each 5 cm high and 3.2 mm thick. Differential pulse height requirements were used to account for the protons which passed through

this counter, and to eliminate them from the experimental trigger. The remaining $\mu^{\pm}$ and $e^{\pm}$ contamination of the beam was carefully measured in Refs. [21,22], and is small at the beam energies used in this experiment. After removal of protons, the fraction of pions in the π^{+} beam was 99.5% and for incident π^{-} the pion fraction varied between 0.97 and 0.98 depending on the energy. The pion fractions from Ref. [21] were used to correct the pion beam count in this experiment. The uncertainty in f_{π} was estimated to be 1%.

The second scintillator S_2 consisted of four 1.6 mm thick vertical adjacent strips each 10 cm high. The two center strips were 8 mm wide while the two outer ones had a width of 12 mm each, such that the intensity was roughly the same on each strip. S_2 was located ~ 90 cm upstream of the target and was used to provide a better definition of the beam at the entrance to the spectrometer.

The incident beam was counted via the coincidence $\overline{S1}\cdot S1\cdot S2\equiv$ beam, where $\overline{S1}$ refers to a veto requirement associated with protons in $S1$, which leave a pulse height in that counter $\geqslant$ four times that of pions. The $S1$ signal also provided the reference time with respect to which the wire chamber drift times were measured, and it defined as well the timing of all the various gates and strobes associated with the spectrometer readout electronics.

If more than one pion was present in a given ~ 4 ns wide beam bucket, the beam coincidence incremented only once. Therefore, the beam count was corrected for this rate dependent effect using Poisson statistics. The technique is described in detail in Refs. [21,23]. The singles fraction is

$$f_s=\frac{\beta\lambda e^{-\lambda}}{1-e^{-\beta\lambda}}, \tag{1}$$

where $\beta=0.85\pm 0.05$ denotes the fraction of the beam which hit $S1$,$S2$, and the target, and with

$$\lambda=\ln\left(\frac{\nu}{\nu-R}\right). \tag{2}$$

Here, the cyclotron rf frequency $\nu=23.058$ MHz, and R is the measured beam rate. Depending on the incident pion energy and polarity, f_s varied from 0.952 to 0.996 in this experiment. The estimated uncertainty in the determination of f_s was only 0.5%.

A veto counter V was placed in the path of the beam at the spectrometer exit. It consisted of two adjacent plastic scintillators each 3 mm thick, and spanned an angular arc of 18° (initiated from the target center).

D. CHAOS

The experiment employed the Canadian High Acceptance Orbit Spectrometer (CHAOS), a magnetic spectrometer designed for pion physics studies [24]. CHAOS consists of a cylindrical dipole magnet, four concentric cylindrical wire chambers (WC1–4), and an array of plastic scintillators and lead glass Cerenkov counters (see Fig. 1). The target was situated at the center of the spectrometer. The CHAOS magnet has a pole diameter of 95 cm, and is capable of producing magnetic fields up to 1.6 T. A 12 cm diameter bore hole along its symmetry axis allowed for the insertion of cryogenic targets. The magnitude of the field was measured with an NMR probe located on the bottom pole face at a radius of about 22 cm. During the experiment, the field setting at $T_{\pi}=284$ MeV was 0.5 T. In order to keep the incident beam trajectory fixed, the ratio of the spectrometer field to the incident momentum was kept constant at all five incident beam energies.

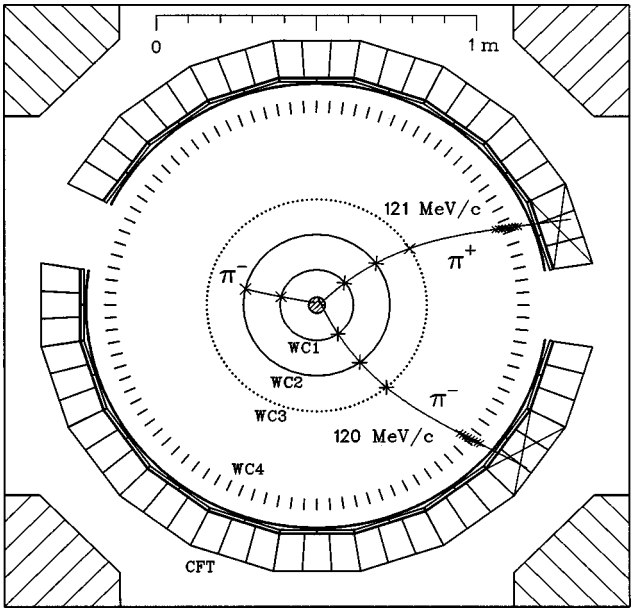

FIG. 1. Illustration of a reconstructed $\pi^{-}p\rightarrow\pi^{+}\pi^{-}n$ event recorded at $T_{\pi^-}=264$ MeV. The profile of the magnet return yokes is visible in the corners. The hit positions in the wire chambers are denoted by crosses. The incident beam is from the left and is registered by hits in WC1 and WC2.

The two inner CHAOS chambers (WC1 and WC2) are multiwire proportional chambers, located at radii of 114 and 229 mm, respectively [24]. An anode pitch of 1/2° is employed for both chambers, which are in addition instrumented with cathode strips inclined 30° with respect to the anodes. WC1 and WC2 are capable of operating at incident beam fluxes of up to ~ 5 MHz without loss of performance.

WC3 is a cylindrical drift chamber located at a radius of 343 mm, designed to operate in a region of high magnetic field. It employs a ''rectangular'' cell geometry [25,26]. In total, there are 144 sense wires, plus 576 cathode strips used to resolve the left/right ambiguity. WC4 is a vector drift chamber with a trapezoidal cell geometry. There are a total of 100 drift cells, each with eight anode drift wires and two additional resistive wires. The drift anodes in each cell are spaced every 5 mm starting from a radius of 613 mm. To resolve the left-right ambiguity, the anode wires are alternately staggered by ± 250 μm in the direction perpendicular to the radial line bisecting the cell. The few cells of WC3 and WC4 which were traversed by the beam were deadened.

The outermost layer of detectors in the spectrometer is a ring of gain stabilized [27] counter telescopes referred to as the CHAOS Fast Trigger (CFT) counters [28]. Each telescope is made up of three layers. The innermost, ΔE_1, is NE110 scintillator 3.5 mm thick with an area of 25 $\times 25$ cm^2; the second layer consists of two adjacent NE110 scintillators (ΔE_{2R} and ΔE_{2L}), each 13 mm thick with a cross sectional area of 13×25 cm^2. The third layer C is

made up of three adjacent lead glass Cerenkov counters, each 12 cm thick with a frontal area of 9.2×25 cm^2. In total there are 20 such counter telescopes, each covering an angular arc of 18°. One such counter was removed where the beam enters the spectrometer, another was replaced by the veto counter V where the beam exited the spectrometer. The solid angle of the spectrometer is therefore determined by the horizontal acceptance of 324°and the vertical acceptance of ±7° defined by the CFT counters ($\sim10\%$ of 4π sr).

E. The experimental trigger

The experiment employed relatively high incident beam rates, and the reaction under study is characterized by cross sections roughly 1000 times smaller than the predominant background reaction, πp elastic scattering. Therefore the success of the experiment relied on use of a powerful trigger system. Two levels of hardware trigger were employed.

The first level trigger (1LT) [28] made use of the scintillation counters. It consisted essentially of a multiplicity requirement on the CFT counters. Each CFT telescope (i) was examined for coincidences in successive layers $[\Delta E_1^i \times(\Delta E_{2L}^i+\Delta E_{2R}^i)]$. The scheme was such that $\Delta E_1^i\times\Delta E_{2L}^i$ was counted as a separate coincidence from $\Delta E_1^i\times\Delta E_{2R}^i$, as was of course also the case for $i\neq j$. Two or more such coincidences were required in coincidence with the 1LT strobe, which was given by beam$\bullet\overline{V}$. The timing of the 1LT was defined by $S1$. Its decision required approximately 100 ns, and the 1LT rate was typically 1 kHz. The 1LT provided the gates, strobes, and common stop signals required by the readout electronics. It also set a busy latch and provided the start for the second level trigger.

The second level trigger (2LT) [29,30] made use of the struck wire information provided by the three innermost wire chambers. This information was processed in a circuit composed primarily of memory lookup units, data stacks, arithmetic logic units, coincidence and delay units all of which were fully programmable. The 2LT searched all combinations of wire numbers in WC1-3 until a combination was found which satisfied all of several predefined criteria. If no such combination was found, the trigger issued a fast clear of the readout system and both triggers were reset. The 2LT filtered events in 2–10 μs based on the following track criteria: the existence of a track defined by hits in the inner three wire chambers separated from one another by less than ±32°, a distance of closest approach to the central axis of not more than 60 mm, and a wide momentum window. In addition two such tracks were required to be found for each event, and the sum of the momenta of the two found tracks (PSUM) was required to be within a range tailored to pass $(\pi,2\pi)$ events at the expense of πp elastic events. The 2LT passed about 10% of the events it received from the 1LT into the data acquisition computer.

In addition to this type of event, two varieties of samples were recorded. One was an unbiased sample of the incident beam, recorded typically at a rate of a few Hz. The other was a sample of the events rejected by the 2LT, also recorded at a few Hz. A detailed description of the CHAOS spectrometer is given in Ref. [24], and some of its subsystems are described in Ref. [28] (the CFT telescopes), Ref. [27] (the CFT gain stabilization system), Refs. [29,30] (the 2LT), Refs. [25,26] (the high field drift chamber WC3), and Ref. [34] (commissioning results).

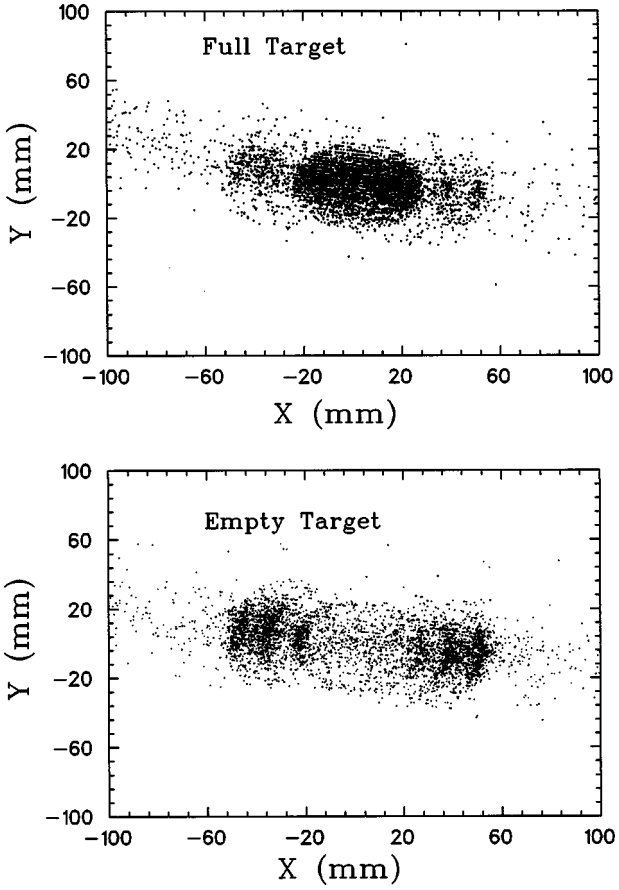

FIG. 2. Horizontal profile of the reconstructed interaction vertex for $\pi^-p\rightarrow\pi^+\pi^-n$ events acquired with the target full (upper, 284 MeV) and empty (lower, 264 MeV).

IV. DATA ANALYSIS

Figure 1 shows a typical $(\pi,2\pi)$ event recorded in the spectrometer. The pion beam is incident from the left, passes through the target located in the center of the spectrometer, and in the absence of a reaction, exits on the right. The position of each incident pion in WC1 and WC2 is recorded. Combined with the known beam momentum, this permits the incident trajectory to be fully reconstructed to the target since the magnetic field is uniform ($\leqslant1\%$) inside WC3. Outgoing tracks are reconstructed using all the available WC information and are similarly extrapolated to the target. The intersection of each outgoing track with the incoming pion trajectory is used to compute the interaction vertex and ''scattering'' angle on an event-by-event basis. The resolution in each of these quantities depends on the scattering angle, but was typically 1.6 mm and 0.5°. The momentum resolution was typically 2% (σ).

Some features of the cryogenic target are visible in Fig. 2 which illustrates the vertex reconstruction provided by CHAOS. These events are primarily elastic scattering events which were passed by the loose trigger conditions employed. The upper part of the figure was acquired with the target full of LH_2, the lower part of the figure with the target empty.

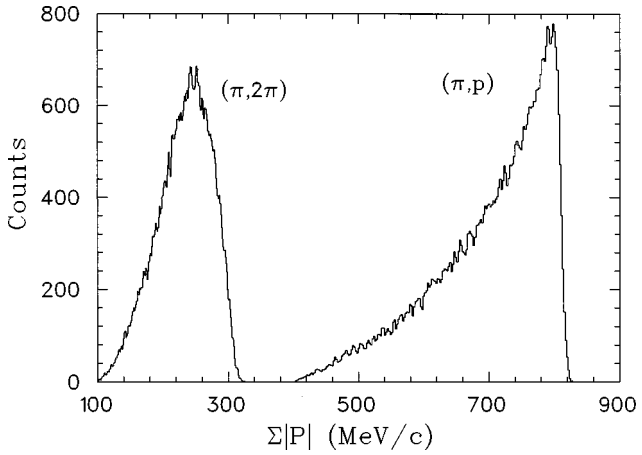

FIG. 3. Momentum sum spectra for πp elastic and $(\pi,2\pi)$ reactions at 285 MeV. The distributions were generated using two- and three-body phase-space.

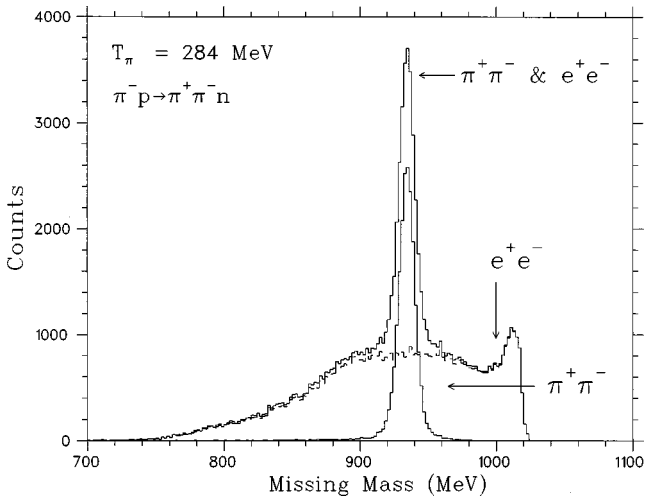

FIG. 4. Missing mass distributions for all events except πp elastic.

The two outer target windows are well separated from events originating in the target cell.

A. Particle identification

Particle identification (PID) was of crucial importance in this experiment. It was achieved [28] by combining the pulse height information from the CFT telescopes with the momentum determined from the wire chambers for each track.

The dominant backgrounds observed were from $\pi^{\pm}p \rightarrow \pi^{\pm}p$ (elastic scattering), and $\pi^{-}p \rightarrow \pi^{0}n$ (SCX). SCX produces background due to the conversion of the π^0 decay photons in the material surrounding the target. This process generates $e^{\pm}$ pairs which imitate $\pi^{\pm}$ pairs. Gamma conversion following $\pi^{-}p \rightarrow \gamma n$ (radiative capture) was also a background source.

Elastic events, although copious, are relatively easily tagged by making use of PSUM and using the observed correlation between the track momentum (p) and pulse height in the ΔE_1 counters. Although in the context of the 2LT PSUM was determined only from the struck wire information of the three innermost chambers, here of course the drift time information of the outer two chambers was used as well. The usefulness of PSUM in this regard is illustrated in Fig. 3, which shows the momentum sum of the two outgoing charged particles for the $(\pi,2\pi)$ and πp elastic reactions, determined from phase space simulations. In the figure the distributions do not reflect the fact that the elastic cross section is roughly three orders of magnitude larger than $(\pi,2\pi)$. However, it is clear from the figure that good separation can be achieved from PSUM constraints.

The $p/\Delta E_1$ correlation is also useful for establishing π/e PID below about 100 MeV/c. Above this momentum, however, the pulse height deposited by π and e tracks in the ΔE_1 counter is nearly the same. In this region, therefore, the Cerenkov information from the lead-glass element of the CFT telescopes was used. Electrons have a much greater bremsstrahlung probability than pions do in the lead glass, leading to showers of Cerenkov light emitting secondary particles. The pulse height observed in the lead glass is correspondingly larger for $e^{\pm}$ than for $\pi^{\pm}$.

To illustrate the ability of the PID system to distinguish pions and electrons, Fig. 4 shows the missing mass determined for a sample of events in which the elastics were already eliminated. The missing mass calculation used in the figure assumed all events were pions. Those identified by the PID algorithms as pions (and those tagged as $e^{\pm}$) are also plotted in the figure. The events tagged as pions show up as a clean, narrow peak ($\sigma = 4.2$ MeV) centered at 946 MeV, (nearly) the expected missing mass of the neutron, and convincingly demonstrate the clean PID achieved as well as the excellent missing mass resolution obtained in this experiment.

B. Acceptance determination

The $\pi,2\pi$ events were isolated from the raw data using constraints on the interaction vertex, PSUM, PID correlations, and the missing mass. The surviving events were characterized in terms of the variables $m_{\pi\pi}$ (the dipion invariant mass), t (the square of the four-momentum transfer to the nucleon), θ (the angle between the two negative pions in the dipion rest frame), and x (the angle between the dipion and the plane defined by the incident pion and the scattered nucleon). We express $m^2_{\pi\pi}$ and t in units of the pion mass squared (μ^2).

Since the out-of-plane acceptance of CHAOS is limited ($\pm 7°$), and the number of experimental events was relatively low, the formation of an event lattice based on four variables was impractical. Consequently, the event lattice was determined in terms of $m_{\pi\pi}$, t, and θ only, all of which are extensively covered by CHAOS. The poorly covered out-of-plane variable x was assumed to be distributed according to three body phase space.

The out-of-plane behavior of the $\pi^{-}p \rightarrow \pi^{+}\pi^{-}n$ reaction was studied in Ref. [15]. They observed increasing deviations from phase space as the bombarding energy was raised, by examining the ratio of the measured out-of-plane total cross sections to those that would have been deduced based on the assumption of phase space for the out-of-plane events. For our incident pion energies, these deviations are small, and range from only $\sim 2\%$ at 223 MeV to $\sim 15\%$ at 305 MeV. To further check the ramifications of the phase-space assumption for x, our acceptance corrected $m^2_{\pi\pi}$ distribution at 305 MeV is compared to that measured in the 4π sr

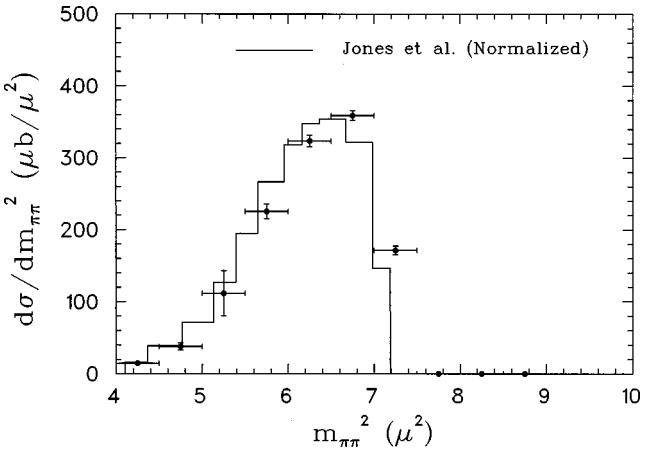

FIG. 5. The acceptance-corrected $m^2_{\pi\pi}$ distribution measured in this experiment for the $(\pi^+\pi^-)$ channel at 305 MeV is represented by the solid points. The horizontal errors indicate the bin width. The line shows the results of Jones *et al.* [8], obtained at 300 MeV in a 4π sr bubble chamber experiment. The Jones data were published in arbitrary units.

bubble chamber experiment of Jones *et al.* [8] in Fig. 5. There is excellent agreement between the shapes of the two distributions, lending further credibility to the assumption that x behaves similar to phase space. Unfortunately, there are no such previous studies at any of the other energies covered in this experiment, or in the $(\pi^+\pi^+)$ channel. A final check related to the phase-space assumption for x is presented in Sec. V, where the total cross sections from this work are compared to previous measurements including results from 4π sr detectors.

Typically 10 000 $\pi^+\pi^\pm$ events were obtained at each energy. All events were binned into a $10\times10\times10$ lattice of $m^2_{\pi\pi}$, t, and $\cos(\theta)$. A weighting factor determined from Monte Carlo simulation of the detector was applied on an event-by-event basis to account for the detector acceptance.

This acceptance correction accounts for the geometrical acceptance of CHAOS, final state pion decay, energy loss, 2LT inefficiency, and track reconstruction inefficiencies. It was determined by using three-body phase-space [31] to generate $(\pi,2\pi)$ events into 4π sr. Each generated event was binned in a lattice of $m^2_{\pi\pi}$, t, and $\cos(\theta)$. Next, the CERN detector simulation package GEANT [32] was employed to track and digitize those generated events which fell within the detector's acceptance. The digitized tracks were then analyzed in exactly the same manner as the experimental data, and each fully reconstructed event was binned in a second lattice. The acceptance correction factor A for a given bin was determined from the ratio of the reconstructed events to the generated ones in that bin.

It is important to note that this procedure does not make any assumptions about the distributions of $m^2_{\pi\pi}$, t, or $\cos(\theta)$. Phase space merely provides a convenient method of generating multiparticle final states which conserve energy and momentum. The only assumption is that x is distributed according to phase space.

Approximately 10^5 events were simulated at each incident pion energy, for both reaction channels. To check the quality of the detector simulation achieved, missing mass spectra for the simulated and the experimental data were compared. The two distributions agree almost perfectly ($\Delta\mu<1$ MeV, $\Delta\sigma\leqslant0.2$ MeV).

C. Cross sections

At a given incident beam energy, the triple differential cross section for $\pi N\rightarrow\pi\pi N$ can be expressed as

$$\frac{\partial^3\sigma}{\partial m^2_{\pi\pi}\partial t\,\partial\cos(\theta)} = \frac{N[m^2_{\pi\pi},t,\cos(\theta)]}{A[m^2_{\pi\pi},t,\cos(\theta)]N_iN_{\rm tgt}\epsilon\Delta m^2_{\pi\pi}\Delta t\Delta\cos(\theta)}, \tag{3}$$

where N is the number of reconstructed events in a given bin of $m^2_{\pi\pi}$, t, and $\cos(\theta)$, N_i is the number of incident pions on target, accounting for the small fraction of multiple pions per beam bucket and the fraction of pions in the beam. $N_{\rm tgt}$ denotes the effective number of target protons per unit area. ϵ represents the overall detection efficiency, which includes the wire chamber efficiencies, computer live-time, and PID efficiency. A is the acceptance correction factor (weight) corresponding to a given bin, and $\Delta m^2_{\pi\pi}$, Δt, and $\Delta\cos(\theta)$ are the bin widths in $m^2_{\pi\pi}$, t, and $\cos(\theta)$, respectively.

Although the normalization quantities found in Eq. (3) were determined individually in order to produce absolute differential cross sections for $\pi N\rightarrow\pi\pi N$, $\pi^\pm p$ elastic scattering data acquired during the experiment were used to provide an independent check on the normalization. In the π^-p channel, elastic data were acquired at 223, 243, and 264 MeV. π^+p elastic scattering events were recorded at all five incident pion energies. From a comparison of the measured elastic differential cross sections and predictions from partial wave analyses [33], it is clear that the overall normalization of the (πp) cross sections is accurate to better than $\pm10\%$.

During the course of the experiment, empty target data were acquired to measure the background of events coming from the windows of the target vessel and which survived the various cuts. The background data were analyzed in the same way as the foreground (target full) data, and subtracted. For both reaction channels, the background never exceeded 2% of the foreground, and was therefore a small and tractable correction.

The systematic uncertainty of the $(\pi,2\pi)$ results was also estimated to be $\sim10\%$. Some typical values for the factors contributing to this are as follows: the pion fraction of the beam (at 265 MeV) was 0.98 ± 0.01. The target fraction, obtained by folding the incident beam profile over the cylindrical target profile was 0.86 ± 0.02. The particle identification efficiency was 0.90 ± 0.05, and the relative error in the absolute target thickness was $\pm2\%$. The overall WC efficiency, determined from elastic scattering data acquired with a singles trigger, was 0.68 ± 0.059. The uncertainty in the wire chamber efficiency dominates, due to the fact that it was determined from the product $\epsilon_1'\epsilon_2'(\epsilon_1\epsilon_2\epsilon_3)^2$, where ϵ_i denotes the efficiency of wire chamber i, and primes denote the incoming beam. Note $\epsilon_4=1.000\pm0.000$ since each of the WC4 cells was composed of eight independent drift anodes, only three of which must fire to register an unambiguous

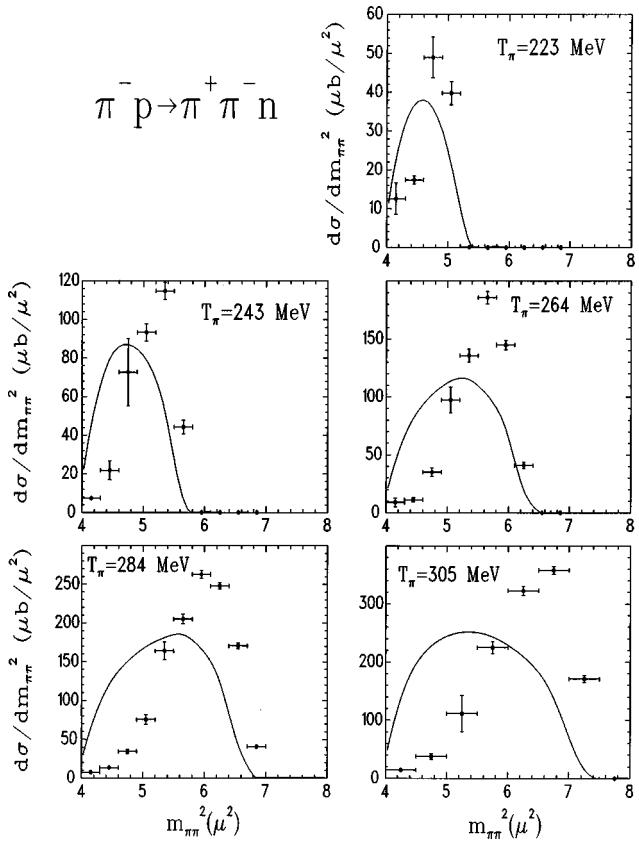

FIG. 6. $m^2_{\pi\pi}$ distributions for $\pi^- p\rightarrow\pi^+\pi^- n$. The solid curves denote the predictions of three-body phase space.

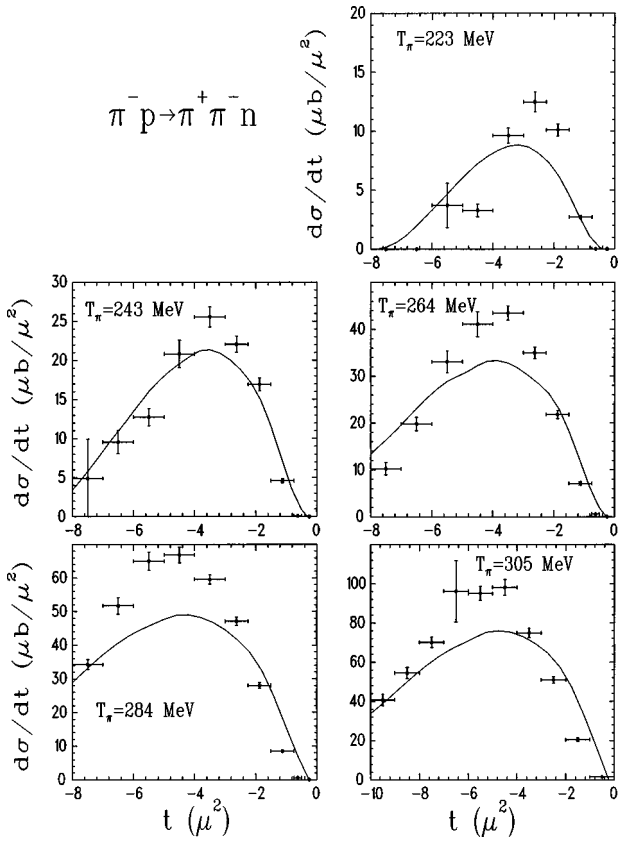

FIG. 7. t distributions for $\pi^- p\rightarrow\pi^+\pi^- n$. The solid curves denote the predictions of three-body phase space.

track. Combined in quadrature, the individual components itemized above give $\pm 10.5\%$ for the overall systematic uncertainty. Further details of the experimental procedure and data analysis can be found in Ref. [7].

V. RESULTS

The triple differential cross sections obtained in this experiment cannot be presented in a practical way in this article. A $10\times10\times10$ lattice was used for each reaction at each of five incident energies, therefore there are 10 000 results. These are available from the corresponding author.

Twofold differential cross sections were obtained by integrating out the $\cos(\theta)$ dependence. Since the subsequent Chew-Low and dispersion analysis of $d^2\sigma/dtdm^2_{\pi\pi}$ is rather involved, but draws heavily on the results presented here, this subject is dealt with in a companion article [6].

Figures 6, 7, and 8 show the measured single differential cross sections for the $(\pi^+\pi^-)$ channel, which were obtained by integrating over the two other variables. The same distributions for the $(\pi^+\pi^+)$ channel are shown in Figs. 9, 10, and 11. The distributions shown were determined by integrating the triple differential cross sections over two of the parameters. The vertical error bars reflect the statistical uncertainty only. The horizontal error bars reflect the bin width used. Tables of these results are also available from the corresponding author. Beyond the comparison already shown in Fig. 5, there are no overlapping data from previous experiments with which to compare. The corresponding phase space predictions are also provided in each figure.

The results presented in these figures extend almost all the way to the kinematic minima in each variable. The minimum kinematically allowed $m^2_{\pi\pi}$ is $4\mu^2$, the maximum reflects the total energy available to the system and is seen to increase with increasing bombarding energy. In the case of the four-momentum transfer distributions, the minimum kinematically allowed t varies between $-0.6\mu^2$ and $-0.3\mu^2$.

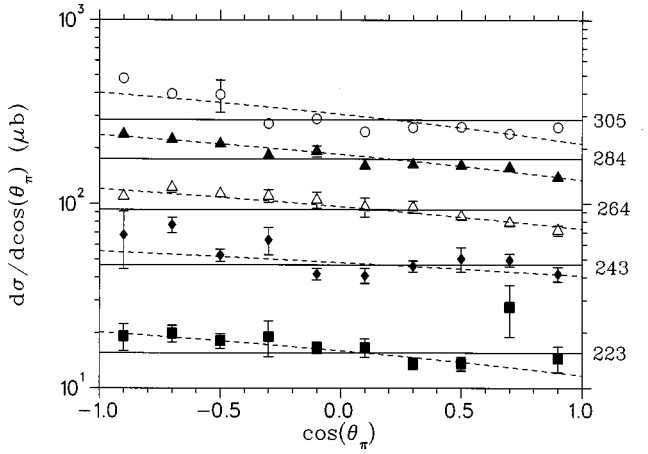

FIG. 8. $\cos(\theta)$ distributions for $\pi^- p\rightarrow\pi^+\pi^- n$. For clarity the horizontal error bars are not shown. The solid lines are best-fit flat lines to the data at each energy, and the dotted lines are the best-fit lines including both S and P waves. The data correspond to $T_\pi = 223$ (solid squares), 243 (solid diamonds), 264 (open triangles), 284 (solid triangles), and 305 MeV (open circles).

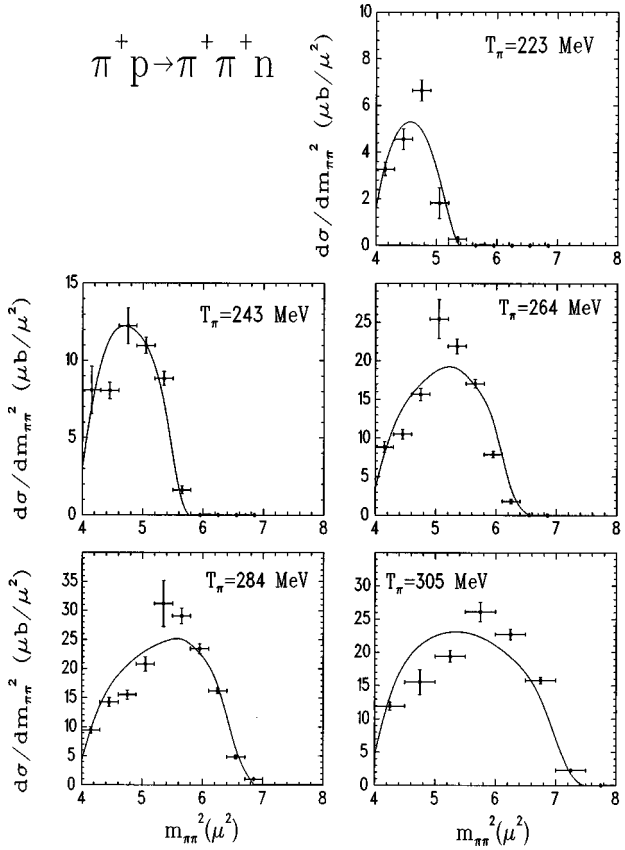

FIG. 9. $m^2_{\pi\pi}$ distributions for $\pi^+ p \to \pi^+ \pi^+ n$. The solid curves denote the predictions of three-body phase space.

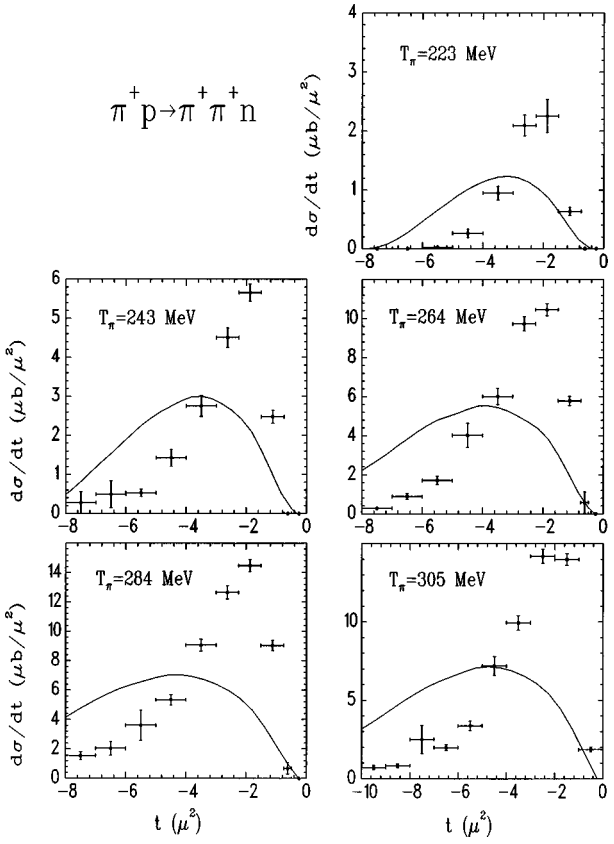

FIG. 10. t distributions for $\pi^+ p \to \pi^+ \pi^+ n$. The solid curves denote the predictions of three-body phase space.

The angular distributions are useful indicators of the reaction mechanism since the OPE contribution should be S wave. Phase-space also predicts isotropic angular distributions, of course. A simple partial wave decomposition was performed on the $\cos(\theta)$ distributions presented in Figs. 8 and 11. For both figures, the best-fit flat lines (S wave only) are shown as well as best-fit curves including S- and P-wave contributions [for $(\pi^+\pi^-)$, Fig. 8], or S- $(P-)$ and D-wave contributions [for $(\pi^+\pi^+)$, Fig. 11]. In the case of the $(\pi^+\pi^-)$ distributions, the P-wave scattering amplitude is between 5 and 10 % of the S-wave amplitude, depending on the energy. In the case of the $(\pi^+\pi^+)$ distributions, the P-wave contribution was consistent with zero, as it must be for a final state with two identical pions. The D-wave scattering amplitude was found to vary between 5 and 15 % of the S-wave amplitude, depending on the energy.

Total cross sections were obtained by integrating the triple differential cross sections over all three variables. Recall that the fourth variable x was assumed to be distributed according to phase space. As such, a comparison of our total cross sections to the results of other groups [8,9,11–14,18,35–43] provides an important check on the validity of the out-of-plane assumption used in the present work. Our results are tabulated in Table I. Figures 12 and 13 show the experimental total cross sections as a function of the incident beam momentum, along with the results from previous experiments. The error bars shown on the graphs (for our results) are the systematic error (the statistical errors are small compared to the systematic error). Here, the horizontal error bars reflect the incident momentum spread. The momenta listed represent the incident pion momentum at the center of the target.

In the $(\pi^+\pi^-)$ channel, the measured total cross sections are consistent with results of previous experiments. The $(\pi^+\pi^+)$ data on the other hand, disagree with the Omicron results [11] below 400 MeV/c. However, the Sevior data [12] also suggest that the Omicron cross sections are too

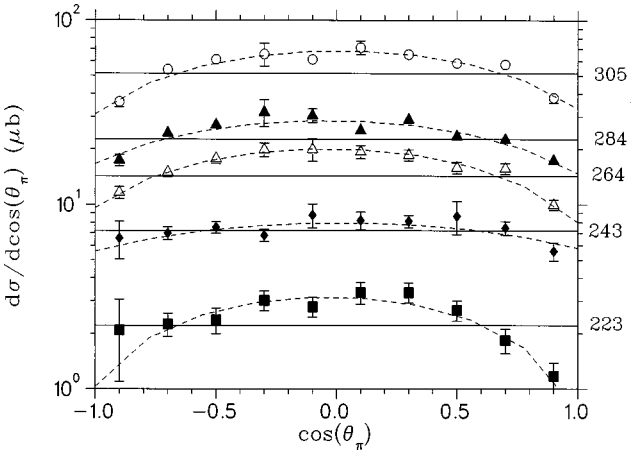

FIG. 11. $\cos(\theta)$ distributions for $\pi^+ p \to \pi^+ \pi^+ n$. For clarity the horizontal error bars are not shown. The 305 MeV results have been multiplied by a factor of 2 for clarity in the figure. The solid lines are best-fit flat lines to the data at each energy, and the dotted lines are the best-fit lines including S (P) and D waves. The data correspond to T_π=223 (solid squares), 243 (solid diamonds), 264 (open triangles), 284 (solid triangles), and 305 MeV (open circles).

TABLE I. Table showing the measured total cross sections. The uncertainty given in the incident momentum column reflects that associated with the mean of the central incident momentum. $\delta\sigma_{\text{stat}}$ refers to the statistical uncertainty, $\delta\sigma_{\text{syst}}$ to the systematic uncertainty.

Reaction channel	Incident T_π (MeV)	Incident p_π (MeV/c)	$\sigma_t(\mu\text{b})$	$\delta\sigma_{\text{stat}}$	$\delta\sigma_{\text{sys}}$
$(\pi^+\pi^+)$	223	335±3.4	5.0	0.3	0.5
$(\pi^+\pi^+)$	243	357±3.6	14.9	0.7	1.4
$(\pi^+\pi^+)$	264	378±3.8	32.7	0.9	3.1
$(\pi^+\pi^+)$	284	400±4.0	49.7	1.4	4.8
$(\pi^+\pi^+)$	305	422±4.2	56.8	1.4	5.4
$(\pi^+\pi^-)$	223	336±2.9	35.6	2.1	4.0
$(\pi^+\pi^-)$	243	357±3.4	106.2	5.8	11.3
$(\pi^+\pi^-)$	264	377±4.0	198.0	4.6	21.0
$(\pi^+\pi^-)$	284	400±4.6	366.5	5.0	34.2
$(\pi^+\pi^-)$	305	422±4.7	620.0	17.0	58.0

high. The solid curve is the predicted cross section obtained from an amplitude fit for all isospin channels of the $\pi N\rightarrow\pi\pi N$ reaction [36]. It indicates that the CHAOS results are consistent with the total cross sections measured by Sevior *et al.* [12] as well as the bulk of previously published cross sections.

VI. INTERPRETATION

The results of this experiment are interpreted with an isobar model, first developed by Oset and Vicente-Vacas [3] (OV) and later extended by Sossi *et al.* [4,5,44]. This model was chosen because to date it is the only framework which is not limited to the threshold region.

The OV model of the $\pi^-p\rightarrow\pi^+\pi^-n$ reaction added diagrams involving nucleon Δ and $N^*(1440)$ intermediate states to the OT model [3]. These additional mechanisms may be summarized as $\pi\pi NN$ coupling through P-wave ρ exchange with nucleon and Δ intermediate states, three-point diagrams with nucleon and Δ intermediate states, and two point diagrams with N^* intermediate states and $NN^*\pi\pi S$-wave coupling through ϵ (an isoscalar resonance state also referred to as the σ meson) exchange.

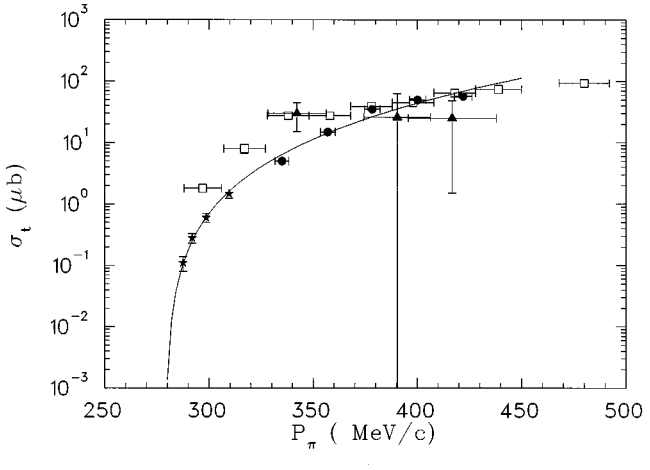

FIG. 12. $\pi^+p\rightarrow\pi^+\pi^+n$ total cross sections from: this work (solid circles), Ref. [11] (open squares), Ref. [12] (solid stars), and Ref. [35] (solid triangles). All previous experimental results shown here were obtained from a comprehensive list presented in Ref. [18]. The solid line is the result of an amplitude analysis performed by Burkhardt and Lowe [36].

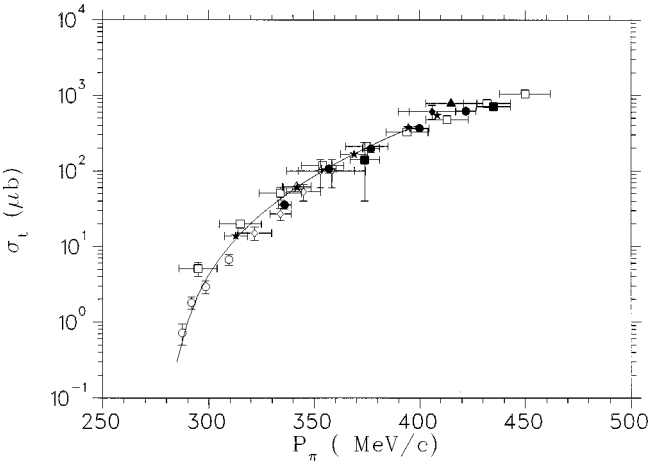

FIG. 13. $\pi^-p\rightarrow\pi^+\pi^-n$ total cross sections from: this work (solid circles), Ref. [9] (open squares), Ref. [37] (solid stars), Refs. [38–40] (open diamonds), Ref. [41] (solid squares), Ref. [42] (solid diamonds), Ref. [13] (open circles), Ref. [43] (open triangles), and Ref. [8] (solid triangles). Results of previous experiments were obtained from a comprehensive list presented in Ref. [18]. The solid line is the result of an amplitude analysis performed by Burkhardt and Lowe [36].

OV assumed that the Lagrangian density for $NN^*\pi\pi$ was given by

$$\mathcal{L}_{NN^*\pi\pi}=-C\bar{\psi}_{N^*}\phi\cdot\phi\psi_N+\text{H.c.} \tag{4}$$

where ψ_{N^*}, ϕ, and ψ_N are the N^*, pion, and nucleon fields, respectively [3]. C is a parameter of the model determined in the original work of OV by estimating the fraction of the width for $N^*\rightarrow\pi\pi N$ which goes into the $N\epsilon$ channel [3]. They estimated C to be $0.91\pm0.20\mu^{-1}$.

Subsequently, Sossi *et al.* [44,5] added P-wave $NN^*\pi\pi$ coupling and replaced the $\pi\pi$ scattering amplitudes in the original OV model with those obtained by Donoghue *et al.* [45] to one-loop order in chiral perturbation theory. The $\pi\pi$ amplitudes in the original OV model were based on the Weinberg $\pi\pi$ Lagrangian, which included the chiral symmetry breaking parameter ξ. Use of the Donoghue amplitudes eliminates the controversial ξ, but involves two additional parameters $\tilde{\alpha}_1$ and $\tilde{\alpha}_2$ which are renormalization constants that must be determined from experimental data.

In the original model [3], the strength of the $N^*\rightarrow N(\pi\pi)_{S\text{-wave}}$ process was not accurately determined [5]. A determination of this quantity requires knowledge of C and the $N^*N\pi$ coupling constant $g_{N^*N\pi}$. The addition of the $N^*\rightarrow N(\pi\pi)_{P\text{-wave}}$ mechanism requires the determination of the $N^*\Delta\pi$ coupling constant $g_{N^*\Delta\pi}$.

The extended OV model [5] was used to compute the $m^2_{\pi\pi}$ distributions for the $(\pi^+\pi^-)$ channel at all five incident energies. The CERN minimization package MINUIT was employed to perform a global fit (at all incident energies simultaneously) of the experimental $m^2_{\pi\pi}$ distributions by

TABLE II. Table showing the results of the global fit to the $(\pi^+\pi^-)$ data, compared to other results.

Reference	$C(\mu^{-1})$	$g_{N^*\Delta\pi}$ (μ^{-1})	$\tilde{\alpha}_1$
[3]	-0.91 ± 0.2		
[47]	-2.07 ± 0.04		
[44]		1.35 ± 0.225	
[5]	-3.04		
[45]			-0.007 ± 0.011
[48]	-1.82		
this work	-1.35 ± 0.001	2.0 ± 0.01	0.017 ± 0.005

varying $\tilde{\alpha}_1$, $\tilde{\alpha}_2$, C, $g_{N^*N\pi}$, and $g_{N^*\Delta\pi}$. Initial studies indicated that the χ^2 of the global fit did not show a strong dependence on $\tilde{\alpha}_2$ or $g_{N^*N\pi}$. Consequently, $\tilde{\alpha}_2$ was fixed at the value given in Ref. [45] (0.013) and $g_{N^*N\pi}$ was set to $0.02\mu^{-1}$ [3,5].

The results of the fit are listed in Table II, and the fits to the $m^2_{\pi\pi}$ distributions and the predicted total cross sections along with their experimental counterparts are shown in Figs. 14 and 15, respectively. The reduced χ^2_ν for the global fit was 10.8. The uncertainty in each parameter was determined from the change in that parameter that caused the χ^2 to increase by 1. These errors were negligible (on the order of 10^{-3}), however, they do not represent the systematic uncertainties present in the model. Given the large χ^2_ν, the systematic errors may be substantial.

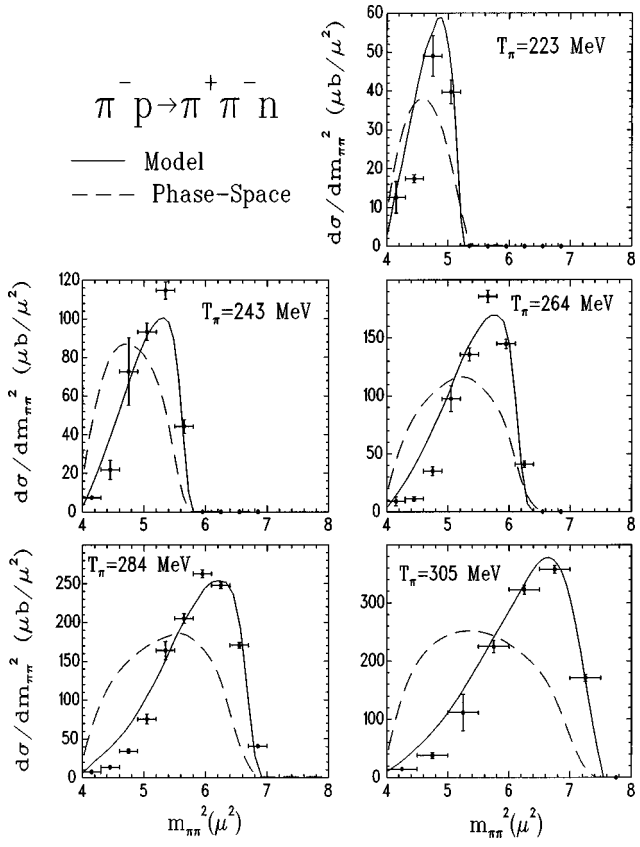

FIG. 14. Measured differential cross sections (solid points) and extended OV model fits (solid lines) for the $(\pi^+\pi^-)$ channel. The dashed lines represent three-body phase-space. The model predictions are absolute, and the phase-space curve has been normalized to the experimental total cross sections.

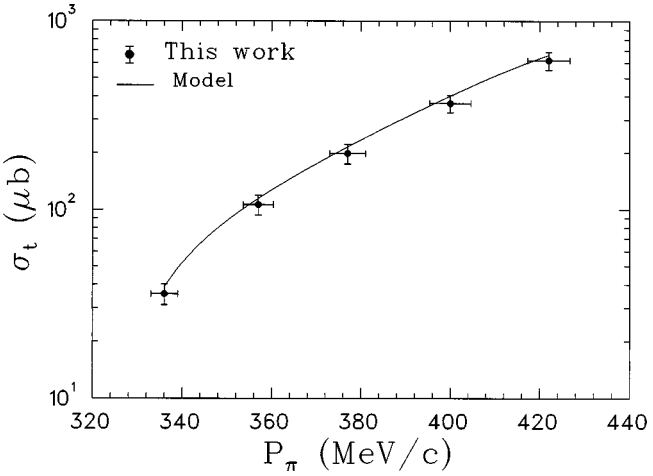

FIG. 15. Illustration of the experimental total cross sections and predictions of the extended OV model for the $(\pi^+\pi^-)$ channel.

The value for C obtained in the current work is very different from those obtained by Oset *et al.* [3] and Sossi *et al.* [5]. However, it should be noted that the previously published values of C are not consistent. In their 1993 work, Sossi *et al.* state that inclusion of the Donoghue amplitudes has a dramatic effect on C, and that the value of C obtained with the Weinberg amplitudes is $-1.97\mu^{-1}$ [5]. In Ref. [5], the value of C obtained with the Donoghue amplitudes is $-3.04\mu^{-1}$. References [3] and [5] also state that their value of C is consistent with the $N^*\rightarrow\pi\pi N$ branching ratio. The total width for $N^*\rightarrow\pi\pi N$ is 350 ± 100 MeV, and the fraction of the width for which the final state pions are in a relative S state is $7.5\pm2.5\%$ [46]. Due to the large uncertainties associated with these parameters, the N^* decay width does not provide a stringent constraint on C.

The difference between the values of C (and to some degree, the uncertainties) obtained in Ref. [5] and that determined in this work can be attributed to the extra constraints imposed by the differential cross sections. In the past, the extended OV model has predominantly been used to fit the experimental total cross sections [5,44]. In general, the parameters determined by fitting the experimental total cross sections may not be well suited towards describing the $m^2_{\pi\pi}$distributions. The invariant mass distributions contain new information concerning the reaction mechanism and place extra constraints on the model.

In order to test the predictive power of the extended OV formalism, the results of the model for the $(\pi^+\pi^+)$ channel using the parameters determined from the $(\pi^+\pi^-)$ data are shown in Fig. 16. The predicted total cross sections are shown in Fig. 17. There is significant disagreement between the experimental results and the model predictions in the $(\pi^+\pi^+)$ channel. Figures 16 and 17 indicate that the model parameters required to describe the $m^2_{\pi\pi}$ distributions in the $(\pi^+\pi^+)$ channel are not consistent with those obtained by fitting the $(\pi^+\pi^-)$ distributions. The $(\pi^+\pi^+)$ data seem to be better described by three body phase space. Coupled with the large χ^2_ν in the $(\pi^+\pi^-)$ channel, the inability of the model to correctly predict the corresponding invariant mass distribution and total cross section in the $(\pi^+\pi^+)$ channel

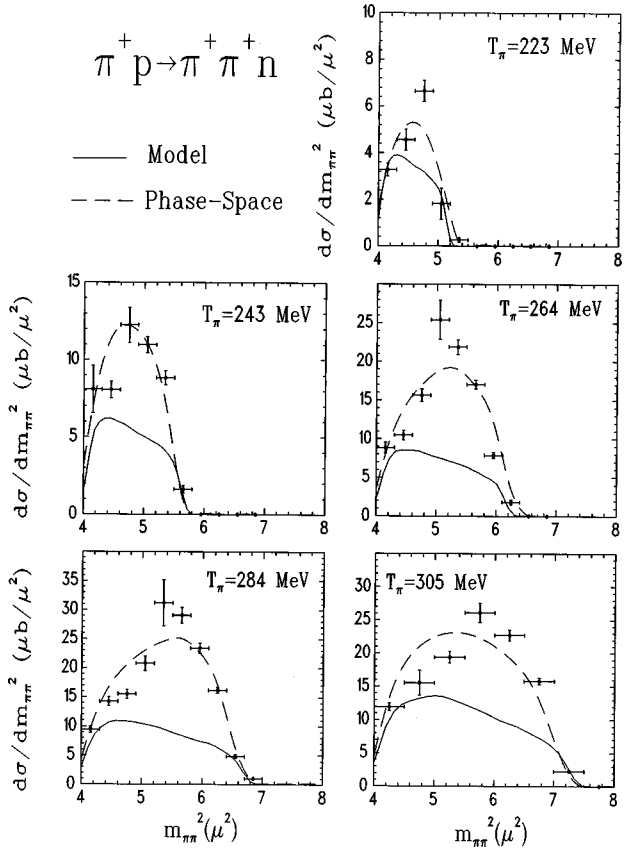

FIG. 16. Measured differential cross sections (solid points) and predictions of the extended OV model (solid lines) for the $(\pi^+\pi^+)$ channel. Three-body phase space is represented by the dashed lines. The phase space curve has been normalized to the experimental total cross sections. The model predictions are absolute.

indicates the fitted parameters obtained in this work are unreliable, and that the model itself is inadequate in its present form.

The extended OV model has been criticized in the work of Olssen, Meissner, Bernard, and Kaiser [49], where they state that the model is inconsistent because the $\pi\pi$ and $\pi\pi N$ amplitudes are not treated at the same order in the chiral expansion, and because the mesonic low energy constants

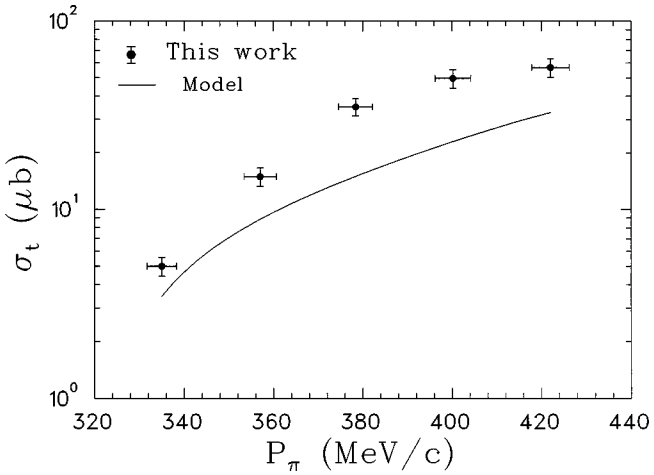

FIG. 17. The experimental total cross sections and predictions of the extended OV model for the $(\pi^+\pi^+)$ channel are shown.

($\tilde{\alpha}_1$ and $\tilde{\alpha}_2$) determined in Ref. [45] were obtained from data over an energy range which clearly exceeds the validity of the one-loop calculation. Prior to a more extensive fit and in order to obtain reliable values of C, $\tilde{\alpha}_1$, and $g_{N*\Delta\pi}$, more theoretical input to the model is clearly required.

VII. CONCLUSIONS

We have performed an exclusive study of the elementary pion induced pion production reactions $\pi^- p \to \pi^+ \pi^- n$ and $\pi^+ p \to \pi^+ \pi^+ n$ at incident pion energies of 223, 243, 264, 284, and 305 MeV. A cryogenic liquid hydrogen target was employed, and the CHAOS magnetic spectrometer was used to detect the two outgoing charged pions in coincidence. On the order of 2000 to 12 000 $(\pi,2\pi)$events were recorded at each energy. The experimental distributions were corrected for detector acceptance and experimental efficiencies in order to produce single, double, and triple differential cross sections for both reaction channels. The overall normalization of the measured distributions was confirmed by comparing our measured absolute differential cross sections for πp elastic scattering to those obtained from phase-shift predictions [33].

The extended Oset and Vicente-Vacas (OV) model [3–5] was used to fit the experimental $m_{\pi\pi}^2$ distributions in the $(\pi^+\pi^-)$ channel. In this analysis, the parameters of the model, namely, C, $g_{N*\Delta\pi}$, and $\tilde{\alpha}_1$ were varied in order to best describe the measured distributions. The resulting parameters do not agree with previous values determined by fitting total cross sections (see Table II). The model parameters obtained from the $(\pi^+\pi^-)$ data were then used to predict the $m_{\pi\pi}^2$ distributions for the $\pi^+ p \to \pi^+ \pi^+ n$ reaction. There is significant disagreement between the model predictions and the experimental data in this channel, highlighting the need for more theoretical effort in this area.

Despite the theoretical uncertainties present in relating the large body of existing $(\pi,2\pi)$ cross sections to $\pi\pi$ scattering observables, the cross sections measured in this work represent the world's most complete data set on pion induced pion production near threshold. The many-fold differential cross sections measured in this work should prove to be of great importance in furthering the understanding of the reaction mechanism involved in $(\pi,2\pi)$. In particular, we have shown that there are significant differences between the reaction mechanisms for the $(\pi^+\pi^+)$ and $(\pi^+\pi^-)$ channels. The theoretical framework used to interpret the data is clearly inadequate. Phase space, which describes the $\pi^+\pi^+$ data rather well, does not describe the $\pi^+\pi^-$ results at all.

Progress is being made in extending the predictions of chiral perturbation theory to the energy regime covered by this experiment [2]. The data presented here should provide a stringent test of the success of that effort.

ACKNOWLEDGMENTS

This work was supported by the Natural Sciences and Engineering Research Council (NSERC) of Canada, as well as by the Instituto Nazionale di Fisica Nucleare (INFN), Italy, and the Australian Research Council. One of us (E.F.G.) acknowledges support from the California State

University Sacramento (CSUS) Foundation. We would also like to thank the technical and support staff of TRIUMF. In particular, the efforts and talents of the cryogenic target group under the leadership of D. Healey are gratefully acknowledged. We also are pleased to acknowledge stimulating discussions and useful remarks from O. Patarakin, D. Počanic, A.A. Bolokhov, M. Shmatikov, and V. Vereshchagin.

[1] S. Weinberg, Phys. Rev. Lett. **7**, 616 (1966); **18**, 188 (1977).
[2] N. Kaiser, *Proceedings of MENU97*, Vancouver, B.C., Canada [πN Newsletter **13**, 308 (1997)].
[3] E. Oset and M. J. Vicente-Vacas, Nucl. Phys. **A446**, 584 (1985).
[4] R. R. Johnson, N. Fazel, N. Suen, and V. Sossi, πN Newsletter **8**, 121 (1993).
[5] V. Sossi, N. Fazel, R. R. Johnson, M. J. Vicente-Vacas, Phys. Lett. B **298**, 287 (1993).
[6] M. A. Kermani *et al.*, Phys. Rev. C **58**, 3431 (1998), following paper.
[7] M. Kermani, Ph.D. thesis, University of British Columbia, 1997.
[8] J. A. Jones, W. W. M. Allison, and D. H. Saxon, Nucl. Phys. **B83**, 93 (1974).
[9] G. Kernel *et al.*, Phys. Lett. B **216**, 244 (1988).
[10] G. Kernel *et al.*, Phys. Lett. B **225**, 198 (1989).
[11] G. Kernel *et al.*, Z. Phys. C **48**, 201 (1990).
[12] M. E. Sevior *et al.*, Phys. Rev. D **48**, 3987 (1993).
[13] J. Lange, Ph.D. thesis, University of British Columbia, 1997.
[14] J. Lange *et al.*, Phys. Rev. Lett. **80**, 1597 (1998).
[15] R. Müller *et al.*, Phys. Rev. C **48**, 981 (1993).
[16] J. Lowe *et al.*, Phys. Rev. C **44**, 956 (1991).
[17] D. Počanić *et al.*, Phys. Rev. Lett. **72**, 1156 (1994).
[18] Emil Frlež, Ph.D. thesis, Los Alamos National Laboratory, Report No. LA-12663-T, 1993.
[19] M. G. Olssen and L. Turner, Phys. Rev. Lett. **20**, 1127 (1968).
[20] Brookhaven National Laboratory, Selected Cryogenic Data Book (unpublished), Vol. I, Sec. III.
[21] M. Pavan, Ph.D. thesis, University of British Columbia, 1995.
[22] G. R. Smith *et al.*, Phys. Rev. C **38**, 240 (1988).
[23] J. T. Brack *et al.*, Phys. Rev. C **41**, 2202 (1990).
[24] G. R. Smith *et al.*, Nucl. Instrum. Methods Phys. Res. A **362**, 349 (1995).
[25] G. J. Hofman, J. T. Brack, P. A. Amaudruz, and G. R. Smith, Nucl. Instrum. Methods Phys. Res. A **325**, 384 (1993).
[26] G. J. Hofman, M.Sc. Thesis, University of British Columbia, 1992.
[27] F. Bonutti, P. Camerini, N. Grion, R. Rui, and P. A. Amaudruz, Nucl. Instrum. Methods Phys. Res. A **337**, 165 (1993).
[28] F. Bonutti, S. Buttazzoni, P. Camerini, N. Grion, R. Rui, Nucl. Instrum. Methods Phys. Res. A **350**, 136 (1994).
[29] S. McFarland, M.Sc. Thesis, University of British Columbia, 1993.
[30] K. J. Raywood, S. J. McFarland, P. A. Amaudruz, G. R. Smith, and M. E. Sevior, Nucl. Instrum. Methods Phys. Res. A **357**, 296 (1995).
[31] FOWL, code obtained from the CERN Program Library, W505.
[32] CERN, GEANT Version 3.21.
[33] R. A. Arndt, Scattering Analysis Interactive Dial-In (SAID). The SM95 solution was used. URL http://clsaid.phys.vt.edu/~CAPS/said_branch.html
[34] M. Kermani, M.Sc. Thesis, University of British Columbia, 1993.
[35] Yu. A. Batusov, S. A. Bunyatov, G. R. Gulkanyan, V. M. Siderov, M. Musakhanov, G. Ionice, E. Losnianu, V. Mihul, and D. Tuvdendorzh, Sov. J. Nucl. Phys. **21**, 162 (1975).
[36] H. Burkhardt, and J. Lowe, Phys. Rev. Lett. **67**, 2622 (1991).
[37] C. W. Bjork *et al.*, Phys. Rev. Lett. **44**, 62 (1980).
[38] Yu. A. Batusov *et al.*, JETP Lett. **12**, 1290 (1961).
[39] Yu. A. Batusov *et al.*, JETP Lett. **16**, 1290 (1961).
[40] Yu. A. Batusov *et al.*, Report No. JINR P-1823, Dubna, 1964.
[41] W. A. Perkins, J. C. Caris, R. W. Kenny, and V. Perez-Mendez, Phys. Rev. **118**, 1364 (1960).
[42] I. M. Blair, H. Müller, G. Torelli, and E. Zavattini, Phys. Lett. **32B**, 528 (1970).
[43] R. Aaron, R. A. Arndt, J. B. Cammarata, D. A. Dicus, and V. L. Teplitz, Phys. Rev. Lett. **44**, 66 (1980).
[44] N. B. Fazel, M.Sc. Thesis, University of British Columbia, 1992.
[45] J. F. Donoghue, C. Ramirez, and G. Valencia, Phys. Rev. D **38**, 2195 (1988).
[46] Particle Data Group, R. M. Barnett *et al.*, Phys. Rev. D **54**, 575 (1996).
[47] V. Sossi *et al.*, Nucl. Phys. **A548**, 562 (1992).
[48] R. Rui, *et al.*, Nucl. Phys. **A517**, 455 (1990).
[49] M. Olssen *et al.*, hep-ph/9503237, 1995.